Duan, R., Liu, W., Xu, L., Huang, Y., Shen, X., Lin, C.-H., Liu, J., Chen, Q., and Sasanapuri, B. 2015 "Mesh type and number for CFD simulations of air distribution in an aircraft cabin," *Numerical Heat Transfer, Part B: Fundamentals*, 67(6), 489-506.

MESH TYPE AND NUMBER FOR CFD SIMULATIONS OF AIR DISTRIBUTION IN AN AIRCRAFT CABIN

Ran Duan[1], Wei Liu[1], Luyi Xu[1], Yan Huang[1], Xiong Shen[1], Chao-Hsin Lin[2], Junjie Liu[1], Qingyan Chen[3,1] and Balasubramanyam Sasanapuri[4]

[1]*Tianjin Key Laboratory of Indoor Air Environmental Quality Control, School of Environmental Science and Engineering, Tianjin University, Tianjin 300072, China*

[2]*Environmental Control Systems, Boeing Commercial Airplanes, Everett, WA 98203, USA*

[3]*School of Mechanical Engineering, Purdue University, West Lafayette, IN 47907, USA*

[4]*ANSYS India Pvt Ltd, Pune, India*

This investigation evaluated the impact of three mesh types (hexahedral, tetrahedral, and hybrid cells) and five grid numbers (3, 6, 12, 24, and >38 million cells) on the accuracy and computing costs of air distribution simulations in a first-class cabin. This study performed numerical error analysis and compared the computed distributions of airflow and temperature. The study found that hexahedral meshes were the most accurate, but the computing costs were also the highest. 12-million-cell hexahedral meshes would produce acceptable numerical results for the first-class cabin. Different mesh types would require different grid numbers in order to generate accurate results.

1. INTRODUCTION

NOMENCLATURE

α_p, α_{nb}	coefficient of the variable at the present cell and neighboring cells, respectively
b	source term or boundary conditions
E_{ro}	maximal round-off error
Err	total numerical error
N	grid number
r_i	distance from the center point of cell i (center of gravity) to the interfacial center f
R_ϕ	normalized residuals
S_ϕ	source term
t	time
x_i	spatial coordinates
$\Gamma_{\phi,eff}$	effective diffusion coefficient
ρ	density of fluid
$\overline{\phi}$	average general variable
ϕ_i^n, $\tilde{\phi}_i^n$	exact solution, approximated solution
ϕ_p, ϕ_{nb}	variable of the present and neighboring cells, respectively
ε_i^n	round-off error

Subscripts and Superscripts

c	center point of cell
f	interfacial center point

[1] Address correspondence to Xiong Shen, Tianjin Key Laboratory of Indoor Air Environmental Quality Control, School of Environmental Science and Engineering, Tianjin University, Tianjin 300072, China. E-mail: shenxiong@tju.edu.cn

TE	truncation error	*i*	index of coordinate
$\overline{u_i}$	average velocity	*nb*	neighboring cells
V	flow domain size	*p*	present cell

In the past decade, the number of air travelers worldwide increased to 11.3 billion [1]. Air distribution in airliner cabins is important for the thermal comfort and well-being of travelers and crew members [2]. However, many recent studies [3, 4] found that thermal comfort in airliner cabins was not satisfactory. The spatial air temperature distributions in airliner cabins were not uniform, and many passengers found that their upper bodies were too warm and lower bodies too cold. Measurements in a large number of commercial airliner cabins by Guan et al. [5] identified many pollutants that are potentially harmful to passengers and crew members and should therefore be removed effectively from the cabins by ventilation. Adjustment of air distribution in cabins in order to improve thermal comfort and reduce pollutant levels is an important subject for airplane cabin designers and researchers.

Experimental measurements and computer simulations are two of the primary methods of investigating air distribution in an airliner cabin [6]. For example, Zhang et al. [7] used a CFD program to study the air distribution in an airliner cabin mock-up. Li et al. [8] measured contaminant distribution experimentally in an airplane cabin. Liu et al. used both experimental measurements [9] and computer simulations [10] to obtain the air distribution in a first-class cabin. These studies showed that, while experimental measurements in an airliner cabin were reliable, it was difficult to conduct the measurements on board with sufficient fine spatial resolution because of regulations imposed by aviation authorities and the high costs associated with the experiments. Most of the measurements were conducted on the ground in airplanes or cabin mock-ups [8, 11, 12]. CFD simulation, on the other hand, is less expensive and more efficient [6]. Thus, recent studies of thermal comfort and air quality in airliner cabins have been conducted primarily by CFD [13-15]. Because the geometry of an airliner cabin is very complex and the airflow appears unstable [10], the experience obtained in simulating airflow in other enclosed spaces, such as buildings, cannot be applied to airliner cabins. Therefore, it is important to investigate the use of CFD for this application.

Significant effort has been made in recent years in studying air distributions in airline cabins by CFD. For example, Liu et al. [10] evaluated different turbulence models for predicting air distributions, and Zhang and Chen [16] assessed various particle models for predicting contaminant dispersions. However, few studies have evaluated the mesh type and number used in CFD. Because CFD solves discretize transport equations for flow (Navier-Stokes equations), the flow domain in an airliner cabin should be divided into a large number of cells. The mesh type and size can be very important factors in the cost of computation and the accuracy of the numerical results.

Since an airliner cabin is three dimensional, the commonly applied mesh types are hexahedral [17], tetrahedral [18], and hybrid meshes [19]. The hexahedron, a structured mesh, was first developed [20] in the 1970s. Compared with tetrahedral and hybrid meshes, hexahedral meshes can be aligned with the predominant direction of a flow, thereby decreasing numerical diffusion [21]. However, it is difficult to generate hexahedral elements for airliner cabins with complicated boundaries [6], although there are examples of this application [17]. Developments in meshing techniques in the 1980s made the tetrahedron a popular alternative [22]. Tetrahedral cells are more adaptive to a flow domain with a complicated boundary [23]. Today, because commercial CFD software can generate tetrahedral meshes automatically, such meshes are favored by inexperienced users. Many researchers [24, 25] have applied these meshes to air cabins. However, a tetrahedron is not as accurate as a hexahedron with the same grid number [26, 27]. The grid number of a tetrahedral mesh is larger than that of a hexahedral mesh with the same cell dimensions. Therefore, hybrid meshes [28, 29] have been developed that use tetrahedral meshes in the flow field with a complicated boundary and hexahedral meshes in the other fluid domain. Several studies [10, 15] have applied hybrid meshes to the investigation of air distributions in cabins. Unfortunately, hybrid meshes cannot be automatically generated, and intensive labor is required to build such a mesh manually.

The above review illustrates the pros and cons of different mesh types. It is important to identify the type mesh that is most suitable for use in airliner cabins.

Another important factor in the computing cost and accuracy of CFD simulations is the number of cells. Many CFD studies have performed grid independence tests. For example, Liu et al. [10] compared three grid quantities for a first-class cabin, but the maximum grid number was only 13 million, which was not sufficiently fine to obtain grid independency. A coarse mesh could lead to a larger spatial discretization error, and refining the mesh could reduce the numerical dissipation. However, if the grid number were very large, round-off error could increase rapidly and would exceed truncation errors, and thus the accuracy could also become poor [30]. Therefore, a cell number that is either too small or too large could lead to poor results. It is necessary to determine the most suitable grid number.

On the basis of state-of-the-art CFD simulations of air distribution in airliner cabins, this investigation conducted a systematic evaluation of mesh type and number. The goal was to identify a suitable mesh type and number for studying air distribution in an airliner cabin in order to improve the thermal comfort and well-being of passengers and crew members.

2. RESEARCH METHOD

2.1. Selection of Grid Type and Number

Our study used the first-class cabin of a single-aisle aircraft (an MD-82 airplane) to study the impact of grid type and number on the computing costs and accuracy of numerical simulations of air distributions in the cabin. Figure 1(a) is a schematic of the fully-occupied, first-class cabin. The role of grid type was investigated by using hexahedral, tetrahedral, and hybrid meshes, as shown in Figure 1. For evaluating grid number, a mesh of at least 3 million cells is necessary in order to describe cabin details that are crucial for simulating air distribution, such as diffusers. We progressively doubled the grid number in order to study its impact on accuracy. Because of limitations on our computing resources, the maximum grid number used was about 48 million. Since it took a long time to generate the finer grids and it was not easy to control the grid number, the largest grid numbers for the hexahedral, tetrahedral, and hybrid meshes were 59, 50, and 38 million, respectively. Table 1 shows the grid numbers used in this investigation.

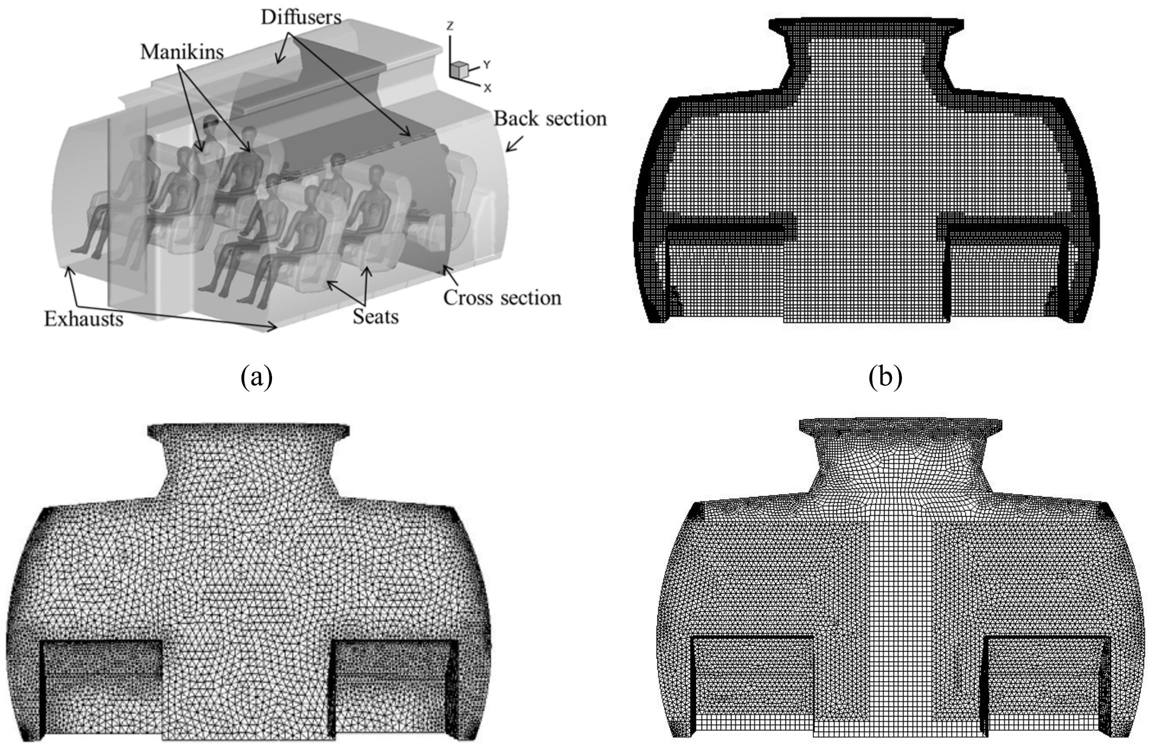

(a) (b)

(c) (d)

Figure 1. (a) Schematic of the fully-occupied, first-class cabin; and mesh distribution at the back section for different mesh grid types: (b) hexahedral mesh, (c) tetrahedral mesh, and (d) hybrid mesh with 24 million cells.

Table 1. Grid numbers, dimensions, and Y+ values used in this study

Mesh type	Abbreviation	Cell number (millions)	Global mesh size (mm)	Surface-average Y+
Hybrid	HY3	3	64	5.02
	HY6	6	48	3.84
	HY12	12	32	3.32
	HY24	24	24	2.86
	HY38	38	24	2.21
Tetrahedral	T3	3	80	4.38
	T6	6	64	3.33
	T12	12	48	2.45
	T24	24	32	2.04
	T50	50	24	1.67
Hexahedral	H12	12	24	2.11
	H24	24	24	1.89
	H59	59	24	1.54

Figure 1 shows the grid distributions of the three mesh types. Different mesh types had similar mesh distributions. For example, the mesh was very fine in the regions close to the walls, manikins, and air diffusers because of large gradients in the variables, while coarse meshes were used in the main flow region. This investigation defined the large mesh dimension used in the main flow region as the global mesh dimension. For the hexahedral mesh, as depicted in Figure 1(b), the distribution of the meshes was uniform in most of the main flow region. Because the diffuser size was only 3 mm and the global mesh dimension was much larger than that, we gradually increased the mesh dimension for the diffusers to the main flow to ensure grid quality. Figure 1(c) shows the tetrahedral mesh distribution and Figure 1(d) the hybrid mesh distribution, under the same strategy as that used for the hexahedral meshes. The hybrid mesh was divided into three flow regions: the region with regular geometry close to the aisle and floor, where hexahedral meshes were used; the region with irregular geometry close to the diffusers, walls, ceiling, seats, and manikins, where tetrahedral meshes were used; and the transition regions, where pyramidal meshes were used.

2.2. Turbulence models and numerical scheme

CFD simulations of air distributions in airliner cabins would need to use turbulence models, as current computer capacity and speed are insufficient to simulate the details of turbulence flow in airliner cabin. Among various turbulence models, Liu et al. [10] recommended large-eddy-simulations (LES) and detached-eddy-simulations (DES) for airflow simulations in airliner cabins. However, these models require long a computing time and high mesh density. Zhang et al. [31] concluded that the LES model provided the most detailed flow features, while the v2f and re-normalization (RNG) k-ε models could produce acceptable results with greatly reduced computing time. Since the RNG k-ε model is one of the most popular turbulence models used in design practice, the current study used this model to simulate cabin flows. Because the airflow in an airliner cabin can be transitional, this study also simulated the flow as transient or unsteady.

The governing equations for the RNG k-ε model for both steady and transient flows can be written in a general form:

$$\rho \frac{\partial \overline{\phi}}{\partial t} + \rho \overline{u}_i \frac{\partial \overline{\phi}}{\partial t} - \frac{\partial}{\partial x_i}[\Gamma_{\phi,eff} \frac{\partial \overline{\phi}}{\partial x_i}] = S_\phi \quad (1)$$

where ϕ represents the flow variables (air velocity, energy, and turbulence parameters), $\Gamma_{\phi,\mathrm{eff}}$ is the effective diffusion coefficient, and S_ϕ is the source term. When $\phi = 1$, then equation (1) becomes the continuity equation.

This study used commercial CFD software FLUENT [32] for all numerical simulations. The Navier-Stokes equation was discretized by the finite-volume method [33, 34, 35]. We employed the SIMPLE algorithm to couple the pressure and velocity calculations. The PRESTO! scheme was adopted for pressure discretization, and the first-order upwind scheme was used for all the other variables. We tested the second-order scheme, but the calculation did not lead to a converged solution [10]; this result was unfortunate, and the scheme should be further investigated in the future. This investigation started an unsteady-state simulation that was based on the results of a steady-state simulation. We estimated that the unsteady-state simulation took one time constant of 50 s to reach a stable flow field. The computation then continued for another 100 s, after which time-averaged simulation results could be obtained.

For the regions near the walls, our study used the enhanced wall function [32], which required that the Y+ value be less than 30. Table 1 shows the surface-averaged wall Y+ values, which were all smaller than 5; thus, the wall function could be used.

The study considered the solutions to be converged when the sum of the normalized residuals for all the cells satisfied the conditions shown in Table 2. The normalized residuals were defined as:

$$R_\phi = \frac{\sum_{cellsP}\left|\sum_{nb} a_{nb}\phi_{nb} + b - a_P\phi_P\right|}{\sum_{cellsP}\left|a_P\phi_P\right|} \tag{2}$$

where ϕ_P and ϕ_{nb} are the given variable at the present and neighboring cells, respectively; a_P is the coefficient of the variable at the present cell; a_{nb} are the correlation coefficients of the variable at the neighboring cells; and b is the source term or boundary conditions.

Table 2. Residual values below which solutions are considered to be converged, for the three different mesh grid types

Residuals	Hexahedral	Tetrahedral	Hybrid
continuity	10^{-4}	10^{-4}	10^{-4}
velocity	10^{-3}	10^{-3}	10^{-3}
energy	10^{-6}	10^{-6}	10^{-6}
k	10^{-3}	10^{-3}	10^{-3}
ε	10^{-4}	10^{-4}	10^{-4}

2.3. Numerical errors

Discretizing the partial differential governing equation (Eq. 1) gives rise to three types of errors: truncation errors, errors introduced by the numerical definitions of boundary conditions, and round-off errors [36]. The following two sub-sections present the method we used to estimate the truncation errors and round-off errors because they are related to grid type and number.

2.3.1. Truncation errors

Figure 2 shows parameters of two adjacent cells and the truncation error between typical neighboring cells for different mesh types. The variable ϕ was chosen as a general variable to account for the truncation error. The variables f and c are the indices of the interfacial and cell center points, respectively. CFD simulations are used to obtain ϕ_f, the ϕ value at f in the interface of two adjacent cells, through interpolation by using the ϕ values at the two cell centers:

$$\phi_{f,i} = \frac{r_{i+1}\phi_{c,i} + r_i\phi_{c,i+1}}{r_i + r_{i+1}} \tag{3}$$

where r_i is the distance from the center of cell i (center of gravity) to the interfacial center point f, and r_{i+1} is the distance from the center of cell i_2 (center of gravity) to the interfacial center point f.

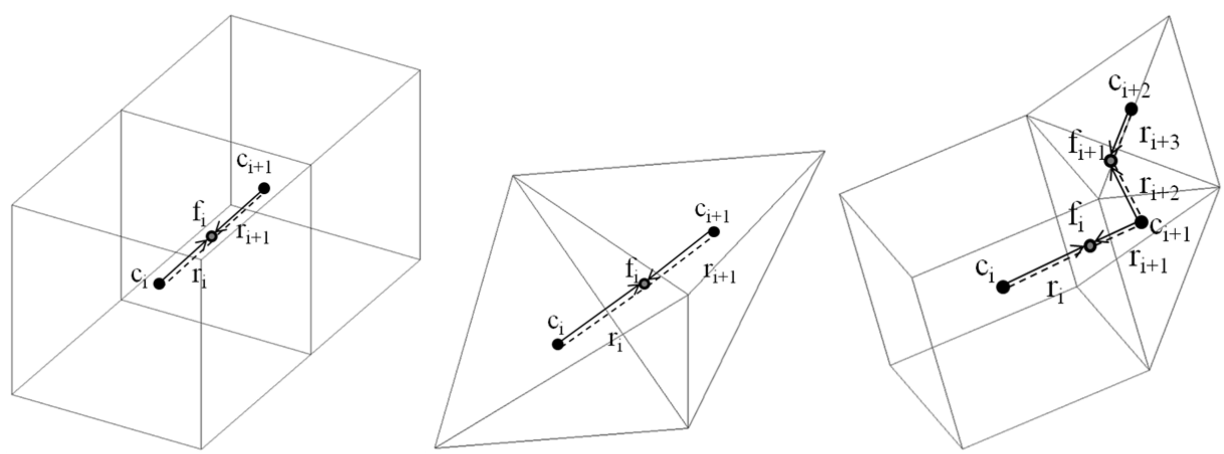

(a) (b) (c)

Figure 2. Typical neighboring cells and parameters of two adjacent cells for different mesh grid types: (a) hexahedral mesh (b) tetrahedral mesh and (c) hybrid mesh.

By using a Tailor series, we can express the term on the right-hand side of Eq. (3) as:

$$r_{i+1}\phi_{c,i} + r_i\phi_{c,i+1} = r_{i+1}\phi_{f,i} + r_i\phi_{f,i} + r_{i+1}(\vec{r}_i \cdot \nabla)\phi_{f,i} + r_i(\vec{r}_{i+1} \cdot \nabla)\phi_{f,i} + r_{i+1}\frac{1}{2!}(\vec{r}_i \cdot \nabla)^2\phi_{f,i} + r_i\frac{1}{2!}(\vec{r}_{i+1} \cdot \nabla)^2\phi_{f,i} + \ldots \tag{4}$$

$$r_i = \left|\vec{r}_i\right|,\ r_{i+1} = \left|\vec{r}_{i+1}\right| \tag{5}$$

Therefore, the truncation error of Eq. (3) is:

$$TE = \frac{r_{i+1}\nabla\phi_{f,i} \cdot \vec{r}_i + r_i\nabla\phi_{f,i} \cdot \vec{r}_{i+1}}{r_i + r_{i+1}} + \frac{1}{2}\frac{r_{i+1}(\vec{r}_i \cdot \nabla)^2\phi_{f,i} + r_i(\vec{r}_{i+1} \cdot \nabla)^2\phi_{f,i}}{r_i + r_{i+1}} + \ldots \tag{6}$$

Let us now study four different grid-type scenarios:

Scenario 1: Neighboring cells have the same geometrical shape and edge length (such as the cubical and equilateral-triangular shaped cells shown in Figures 2(a) and (b), respectively). The directions of r_i and r_{i+1} are opposite one another, and r_{i+1} is thus:

$$\vec{r}_{i+1} = -\vec{r}_i \tag{7}$$

The first term of the truncation error in Eq. (6) becomes zero, so the truncation error is second-order as follows:

$$TE = \frac{1}{2}\frac{r_{i+1}(\vec{r}_i \cdot \nabla)^2\phi_{f,i} + r_i(\vec{r}_{i+1} \cdot \nabla)^2\phi_{f,i}}{r_i + r_{i+1}} + \ldots \tag{8}$$

Scenario 2: Neighboring cells have different geometrical shapes, but each cell has equal edge lengths, such as those shown in Figure 2(c). When hexahedral and pyramidal cells are adjacent to each other, then r_{i+1} can be written as

$$\vec{r}_{i+1} = -\frac{r_{i+1}}{r_i}\vec{r}_i \tag{9}$$

The first term of the truncation error in Eq. (6) again becomes zero, and the truncation error is also of second order. When tetrahedral and pyramidal cells are adjacent to each other, r_{i+2} and r_{i+3} are not parallel. The first term of the truncation error cannot cancel out, and the truncation error will be of first order.

In hybrid meshes with transitions between tetrahedral and pyramidal cells, the truncation error is of first order, while in meshes of a single type such as hexahedral and tetrahedral meshes, the leading term is of second order. Therefore, the truncation error for hybrid meshes will be higher than that for the other two grid types.

Scenario 3: Neighboring cells have the same geometrical shape, but each cell has different edge lengths (such as a rectangular parallelepiped and scalene-triangular shaped cell). The first term of the errors arising on opposite hexahedral cell faces cancels out completely on the basis of Eq. (9), since the cell faces are parallel. However, because the cell faces are not parallel for tetrahedral meshes, the truncation error is still of first order. Hence, hexahedral meshes are superior to tetrahedral meshes with a similar resolution [21].

Scenario 4: Neighboring cells have different geometrical shapes, and each cell has different edge lengths. The truncation error is always of first order.

Refining the meshes would reduce the truncation error. When the mesh is sufficiently fine, mesh type has little influence on the accuracy of simulation results because

$$\lim_{r_i \to 0}(TE) = O(r_i) = 0 \tag{10}$$

2.3.2. Round-off errors

Round-off error, ε_i^n, is the difference between the exact solution ϕ_i^n and the approximated solution $\tilde{\phi}_i^n$ of the governing equation, as shown in Eq. (11). Limited computer word length would lead to the round-off error. As the time step size and cell dimension decrease, the round-off error increases while the truncation error decreases. Decreasing the cell dimension and time step size does ensure more accurate results. When the time step size and cell dimension are very small, the accuracy is compromised because the round-off error may overtake the truncation error. Therefore, the grid number should be small enough to prevent round-off error.

$$\varepsilon_i^n = \phi_i^n - \overline{\phi}_i^n \tag{11}$$

It is necessary to identify the relationship between numerical errors (including round-off and truncation errors) and grid number. Since the cell dimension may not be constant over an entire computational domain because of the uneven mesh distribution, let us use an average cell dimension to estimate the average truncation error. In the case in which r_i and r_{i+1} have the same direction and the second and higher order terms in Eq. (6) can be neglected, the averaged truncation error in the computational domain will be maximal:

$$\overline{TE} = \sqrt[3]{\frac{V}{N}} \times \nabla \phi_f \tag{12}$$

where N is the grid number and V is the flow domain size (15.5 m^3 for the first-class cabin). In the case in which r_i and r_{i+1} have the opposite direction and the second and higher order terms in Eq. (6) can be neglected, the averaged truncation error will be zero.

For a CFD program with double precision parameters, the storage accuracy of a computer can be as high as 10^{-15}. If we iterate 20,000 time steps for a 150 s unsteady-state simulation in the first-class cabin, the maximal round-off error is:

$$E_{ro} = N \times 20{,}000 / 10^{15} \tag{13}$$

The total numerical error is then:

$$Err = N \times 2 \times 10^{-11} + \sqrt[3]{\frac{V}{N}} \times \nabla \phi_f \tag{14}$$

A suitable grid number for achieving the minimal numerical error can be determined by equating the derivative of the right-hand term of Eq. (14) to zero. By using V = 15.5 m^3, we obtain

$$N{=}9.2 \times 10^7 \sqrt[4]{\nabla \phi_f^3} \tag{15}$$

Eq. (15) shows that a suitable grid number is a function of ϕ for the air cabin.

3. RESULTS

This section first compares the simulated results from the steady- and unsteady-state RNG k-ε models with the measured data, and then discusses the impact of mesh type and number on the simulated results.

3.1. Steady- and unsteady-state turbulent flow modeling

The steady-state RNG k-ε model (RANS) and unsteady-state RNG k-ε model (URANS) should yield the same results for stable flow. However, as shown in Figure 3, different air velocity profiles were obtained in the three selected vertical positions in the cabin with hexahedral meshes of 24 million cells. Because the URANS results were obtained by averaging them over 100 s (two time constants), the differences in the two simulated results suggest that the flow in the cabin was unstable. Kumar and Dewan [37] found that thermal plumes can be intermittent and give rise to time-dependent fluctuated flow fields around human bodies. Figure 3 also shows that the prediction by URANS is better than that by RANS when the simulated results are compared with the experimental data. However, it is important to note that the experimental data contained some uncertainties resulting from the complex boundary conditions, as reported by Liu et al. [6]. The experimental data should be used only as a reference, rather than a criterion. Because of the unstable flow features, this investigation used URANS to study the impact of grid type and number on the prediction of air distributions in the airliner cabin.

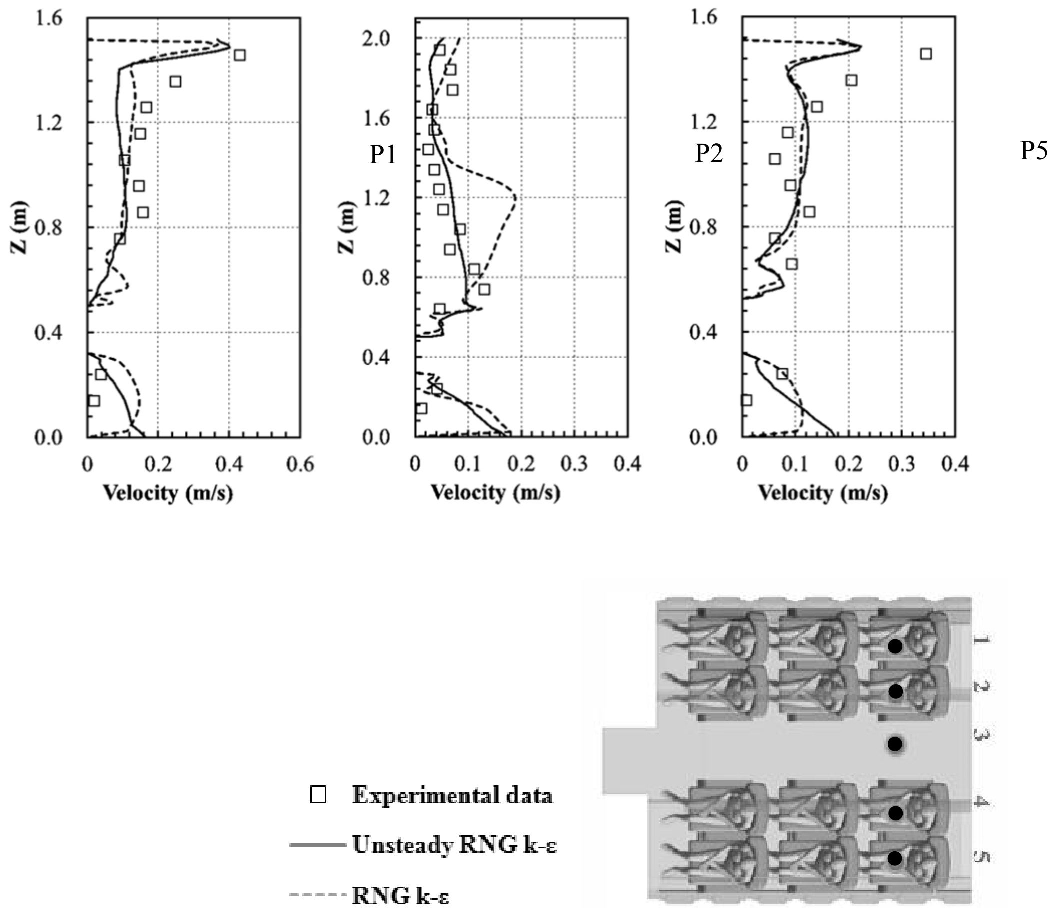

Figure 3. Comparison of the simulated air velocity profiles obtained by the RNG k-ε and unsteady-state RNG k-ε models with those measured in the occupied first-class cabin.

3.2. Impact of grid number on the simulated results

Figure 4 compares the simulated velocity profiles at five vertical sampling lines with tetrahedral meshes of different grid number. As the grid number increased, the truncation error decreased. However, mesh density was high in the regions close to the walls and air diffusers, such as at P1 and P5, and local truncation errors in these regions were smaller. Hence, a further increase in grid number had little influence on the simulated velocity profiles at P1 and P5.

However, in the regions with large cell dimensions, such as at P2, P3, and P4, the corresponding truncation errors were large. The different grid numbers led to different simulated results. The results were very different from those with finer grids, especially when the grid numbers were low (3 and 6 million cells). The simulated air velocity profiles were similar with meshes of 12, 24, and 50 million cells, which meant that the truncation errors were similar.

Figure 4 also shows the measured air velocity profiles at the five vertical positions. The simulated and measured results show similar trends. The differences between the two results can be attributed to numerical errors and experimental uncertainties.

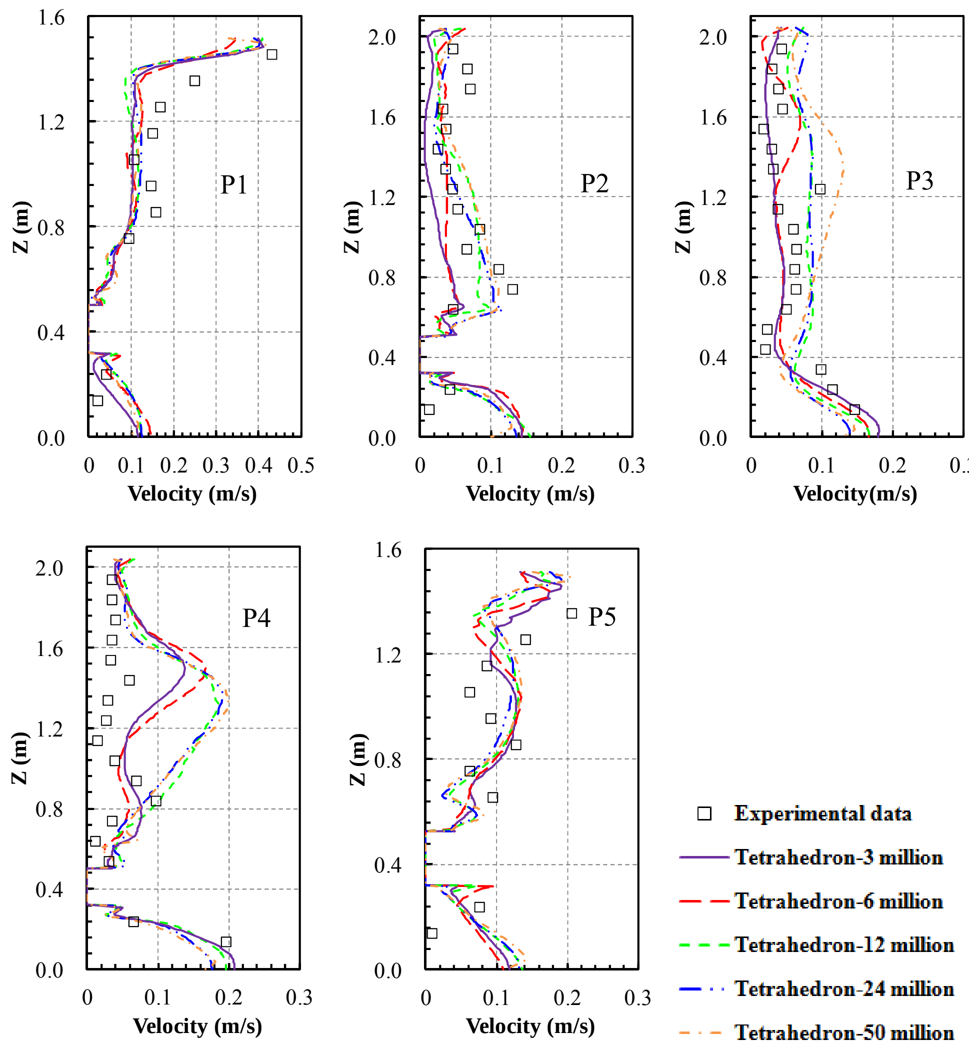

Figure 4. Comparison of the vertical air velocity profiles computed using different tetrahedral meshes with the experimental data at the five locations in the occupied cabin.

Figure 5 compares the simulated temperature profiles at the five vertical lines with tetrahedral meshes of different grid number. The simulated temperature was less affected by truncation errors than was velocity, as a result of the small temperature gradient in the cabin. The temperature profiles for grid numbers of 3 and 6 million cells differed from those for finer grids, although the difference was not as evident for temperature as for velocity.

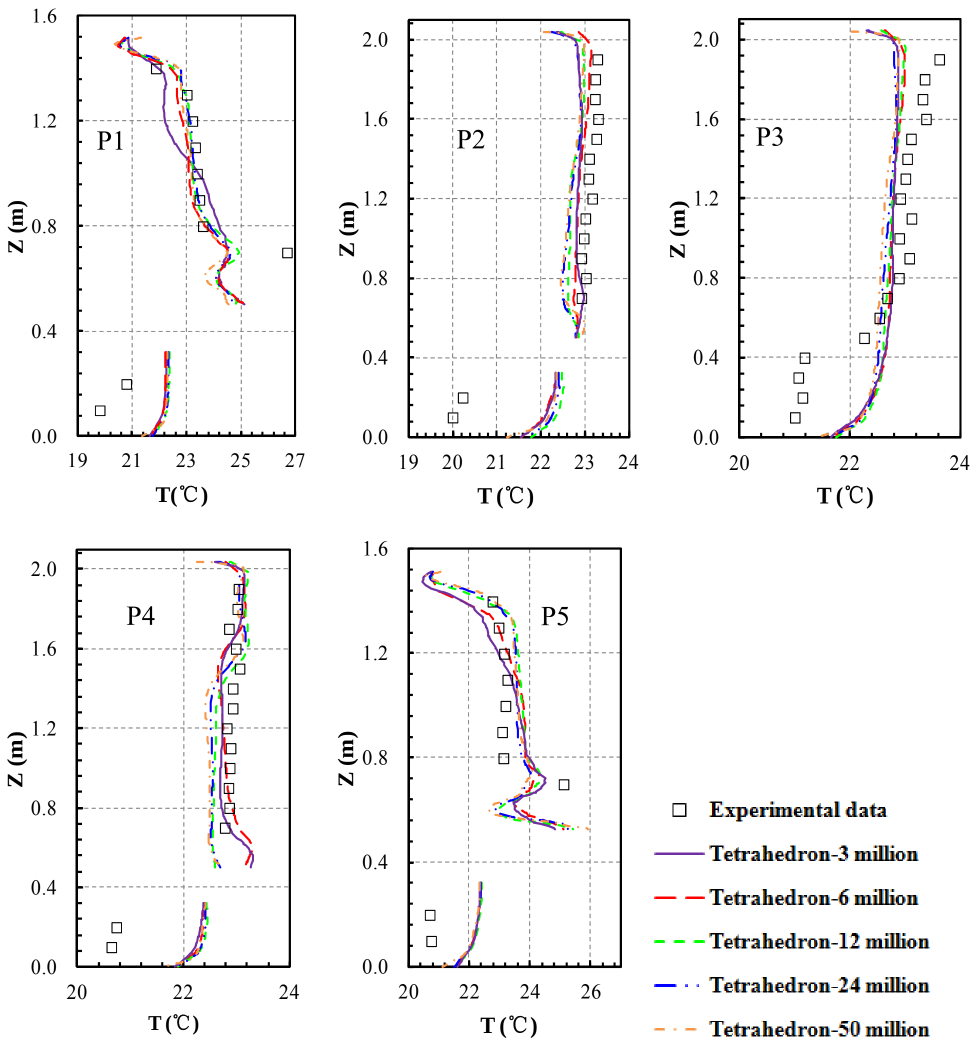

Figure 5. Comparison of the vertical air temperature profiles computed using different tetrahedral meshes with the experimental data at the five locations in the occupied cabin.

Although not discussed in this paper, the results for the hexahedral and hybrid meshes exhibited patterns that were similar to those of the tetrahedral meshes. Because of the complicated geometrical boundary, we found that hexahedral meshes with three million cells were insufficient for generating a reasonable mesh distribution. The corresponding simulations did not lead to converged solutions. A mesh size of at least 12 million cells was required for a hexahedral mesh in the first-class cabin.

3.3. Impact of mesh type on the simulated results

Figure 6 compares the simulated and measured airflow distributions with coarse (3 million cells), medium (12 million cells) and fine (more than 38 million cells) meshes at a cross section in the first-class cabin. (The location of the cross section is shown in Figure 1(a).) Figure 6(a) presents only the results for 3-million-cell tetrahedral and hybrid meshes, because the simulation with 3 million hexahedral cells did not lead to a converged result. Since hybrid meshes have many transitional regions between mesh types, where the truncation errors are large according to Eq. (5), the two airflow patterns obtained with the tetrahedral and hybrid meshes are very different, and one of the hybrid meshes appears to be wrong when compared with the experimental data shown in Figure 6(d).

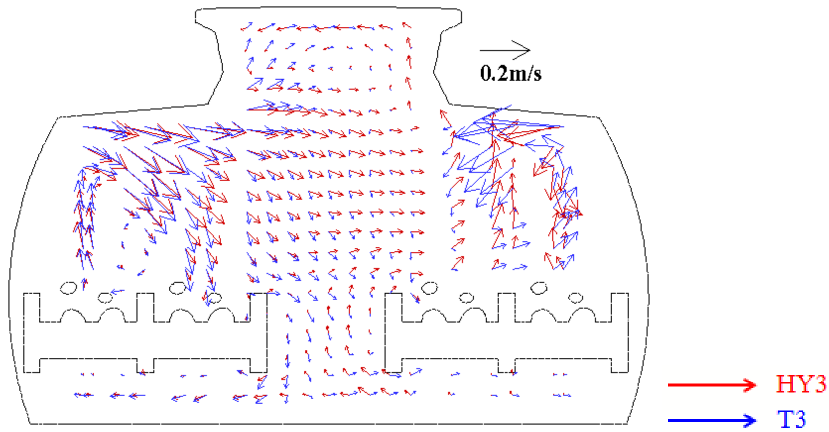

(a) 3 million cells

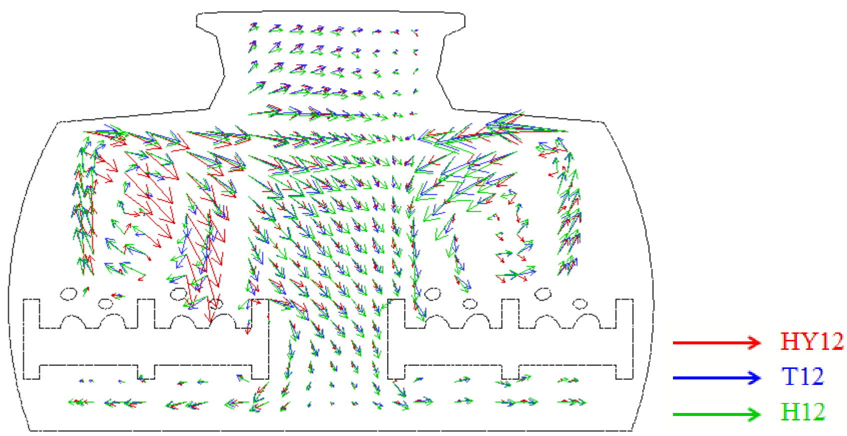

(b) 12 million cells

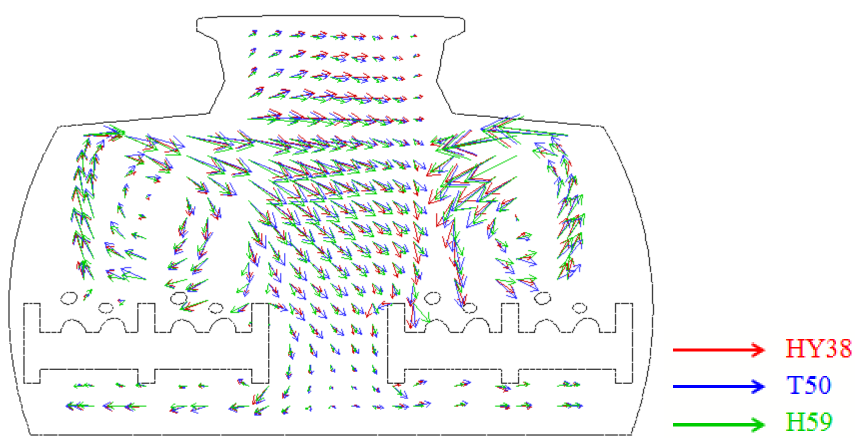

(c) More than 38 million cells

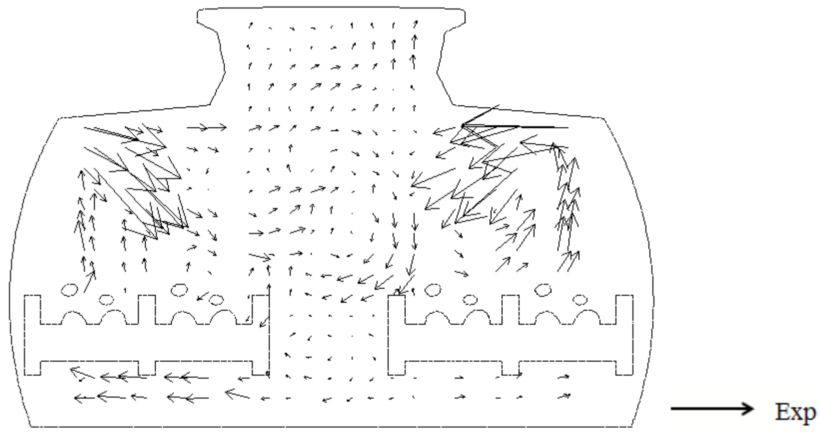

(d) Experimental data

Figure 6. Comparison of the airflow patterns simulated using different grid types and numbers with the experimental data at a cross section in the cabin.

Because of the large cell dimension for T3 (Please see abbreviations for T3, H12, T12, HY3, HY12, etc. in Table 1.), the truncation error was large. The grid resolution and numerical diffusion were insufficient for correctly describing the circulation flow driven by the thermal plumes from the human bodies and the jets from the diffusers on the right side of the cabin. Figure 6(b) shows that H12 and T12 led to reasonable solutions, but HY12 could not predict the circulation on the right side of the cabin. Only when the grid number was sufficiently high did the three mesh types lead to similar results, as shown in Figure 6(c).

Figure 7 compares the simulated and measured temperature fields with different grid types and numbers. Because HY3 did not accurately simulate the jet flow from the diffusers on the right side of the cabin, the air temperature in the region was high. When the grid number was increased, the predicted air temperature distributions agreed well with the measured distribution, as shown in Figure 7(i). Prediction accuracy with the hybrid meshes was poorer than with the other two mesh types, but the differences between simulated and experimental results were not as evident as those for air velocity.

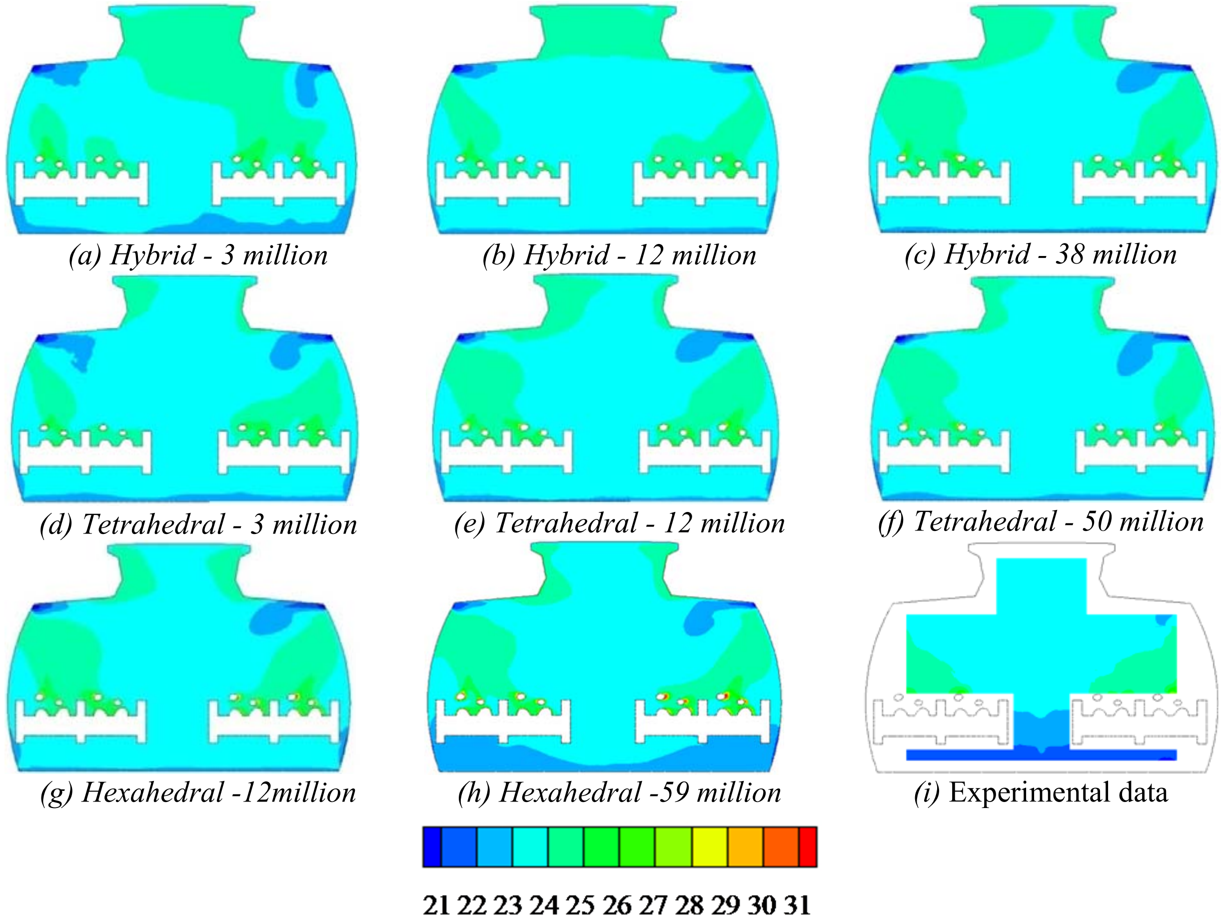

Figure 7. Comparison of the air temperature distributions simulated using different grid types and numbers with the experimental data at a cross section in the cabin.

A comparison of air velocity and temperature distributions showed that, because of truncation errors, different mesh types produced simulation results of varying accuracy. Among the three mesh types, the hexahedral grid had the highest accuracy, while the hybrid grid had the lowest. As the grid number increased, the truncation error decreased. At sufficiently high grid numbers, the effect of mesh type on the simulation results was small.

3.4. Impact of mesh type and grid number on the numerical errors and computing costs

Table 3 shows the numerical errors with the finest hexahedral meshes (H59), which were calculated by Eq. (12, 13). The maximal round-off error was determined by assuming a double precision simulation with a storage accuracy of 10^{-15} and a grid number of 59 million. The truncation error was determined from the gradient distribution of ϕ and cell dimension. When the largest gradient of parameter ϕ in the aisle region with the largest cell dimension was used in this calculation, the maximal truncation error was found to be $0.012\nabla\phi_{f_i}$. Table 3 provides the truncation errors for different ϕ. The round-off errors were comparable to the truncation errors with the finest grid.

Table 3. Analysis of numerical errors

Error	Parameters	Maximum	Medium	Minimum
Truncation error	Velocity	10^{-3}	10^{-4}	0
	Temperature	10^{-2}	10^{-3}	0
Round-off error	All parameters	10^{-3}	n/a	10^{-15}

n/a = not available.

The accuracy of the simulation results for different grids is compared further in Table 5. This study used the relative error between the key predicted and measured results as a criterion and ranked the error in the range of Grade A to Grade D. Grades A, B, C, and D represent relative errors of 0-10%, 10-20%, 20-30%, and greater than 30%, respectively. Table 4 shows that simulations with the hexahedral meshes most closely match the experimental data for both air velocity and temperature. A grid number of at least 12 million cells were necessary for convergence with the hexahedral meshes. When the grid number was increased to more than 38 million, all three grid types had similar results.

Table 4. Accuracy of the simulations with different grid types and numbers

Mesh type	Parameter	Grid number (millions of cells)				
		3	6	12	24	>38
Hybrid	Temperature (^oC)	C	B	B	B	B
	Velocity (m/s)	D	D	D	D	B
Tetrahedral	Temperature (^oC)	C	B	B	B	B
	Velocity (m/s)	D	D	C	C	B
Hexahedral	Temperature (^oC)	n/c		B	B	B
	Velocity (m/s)			B	B	B

A = good (≤10%), B = acceptable (10%, 20%), C = marginal (20%, 30%), D = poor (>30%), n/c = not converged.

Table 5 summarizes the computing time required. All the simulations were performed on a stand-alone computer with 32 cores and 128G memory. It is clear that the larger the grid number, the longer the computing time. The time was nearly proportional to the grid number. The computing time was also related to the node numbers of the cells. The hexahedral meshes had more cells than the tetrahedral meshes, which led to a longer computing time. In addition, the high aspect ratio for the tetrahedral meshes may have influenced computing time. In summary, the hexahedral meshes required the longest computing time, and the hybrid meshes the shortest. The computing time and the accuracy of the simulated results with 24-million-cell hybrid meshes were similar to the time and accuracy, respectively, with 12-million-cell hexahedral meshes. We can apparently conclude that, regardless of the grid type used, similar computing times are required to achieve a given level of accuracy.

Table 5. Computing time for different grid types and numbers

Grid type	Grid number (millions of cells)

	3	6	12	24	>38
Hybrid	10.2h	24.8h	47.0h	92.4h	197.6h
Tetrahedral	15.4h	37.6h	72.8h	141.7h	374.7h
Hexahedral	n/c		81.2h	188.2h	565.5h

n/c = not converged

4. CONCLUSION

This study evaluated the performance of three mesh types and five grid numbers for predicting airflow and temperature distributions in the first-class cabin of an MD-82 airplane. The investigation led to the following conclusions:

The hexahedral meshes were the most accurate, while also being the most time-consuming. The hybrid meshes were the least accurate but used the least computing time. By increasing the grid number of the hybrid mesh to obtain the same accuracy as that with the hexahedral meshes, a similar computing time is achieved. The results suggest that in simulations with 12-million-cell hexahedral meshes, 24-million-cell hybrid meshes, and tetrahedral meshes of approximately 15 million cells, the accuracy would be the same. Furthermore, the computing time for each of these simulations would be about 80-90 hours on the computer cluster used for this investigation.

For the first-class cabin, this study found that a grid number of at least 12 million cells were needed to produce acceptable results. When the grid was sufficiently fine (>38 million cells), all the three mesh types produced similar results.

The truncation errors were typically larger than the round-off errors. When the grid number was sufficiently large (>38 million), the round-off errors were comparable to the truncation errors.

ACKNOWLEDGEMENTS

This study was supported by the National Basic Research Program of China (the 973 Program) through Grant No. 2012CB720100 and the Center for Cabin Air Reformative Environment (CARE) at Tianjin University, China.

REFERENCES

[1] World Bank Group (Ed.), World Development Indicators 2013, World Bank Publications, 2013.

[2] A. Mangili and M. A. Gendreau, Transmission of infectious diseases during commercial air travel, *The Lancet*, vol. 365, pp. 989-996, 2005.

[3] S. Park, R. T. Hellwig, G. Grün and A. Holm, Local and overall thermal comfort in an aircraft cabin and their interrelations, *Building and Environment*, vol. 46, pp. 1056-1064, 2011.

[4] W. Cui, Q. Ouyang and Y. Zhu, Field study of thermal environment spatial distribution and passenger local thermal comfort in aircraft cabin, *Building and Environment*, vol. 80, pp. 213-220, 2014.

[5] J. Guan, C. Wang, K. Gao, X. Yang, C. H. Lin and C. Lu, Measurements of volatile organic compounds in aircraft cabins. Part II: Target list, concentration levels and possible influencing factors, *Building and Environment*, vol. 75, pp. 170-175, 2014.

[6] W. Liu, S. Mazumdar, Z. Zhang, S. B. Poussou, J. Liu, C. H. Lin and Q. Chen, State-of-the-art methods for studying air distributions in commercial airliner cabins, *Building and Environment*, vol. 47, pp. 5-12, 2012.

[7] Z. Zhang, X. Chen, S. Mazumdar, T. Zhang and Q. Chen, Experimental and numerical investigation of airflow and contaminant transport in an airliner cabin mockup, *Building and Environment*, vol. 44, pp. 85-94, 2009.

[8] F. Li, J. Liu, J. Pei, C. H. Lin and Q. Chen, Experimental study of gaseous and particulate contaminants distribution in an aircraft cabin, *Atmospheric Environment*, vol. 85, pp. 223-233, 2014.

[9] W. Liu, J. Wen, J. Chao, W. Yin, C. Shen, D. Lai, C. H. Lin, J. Liu, H. Sun and Q. Chen, Accurate and high-resolution boundary conditions and flow fields in the first-class cabin of an MD-82 commercial airliner, *Atmospheric Environment*, vol. 56, pp. 33-44, 2012.

[10] W. Liu, J. Wen, C. H. Lin, J. Liu, Z. Long and Q. Chen, Evaluation of various categories of turbulence models for predicting air distribution in an airliner cabin, *Building and Environment*, vol. 65, pp. 118-131, 2013.

[11] T. T. Zhang, P. Li and S. Wang, A personal air distribution system with air terminals embedded in chair armrests on commercial airplanes, *Building and Environment*, vol. 47, pp. 89-99, 2012.

[12] A. Wang, Y. Zhang, Y. Sun and X. Wang, Experimental study of ventilation effectiveness and air velocity distribution in an aircraft cabin mockup, *Building and Environment*, vol. 43, pp. 337-343, 2008.

[13] M. Wang, C. H. Lin and Q. Chen, Determination of particle deposition in enclosed spaces by Detached Eddy Simulation with the Lagrangian method, *Atmospheric Environment*, vol. 45, pp. 5376-5384, 2011.

[14] C. Chen, W. Liu, F. Li, C. H. Lin, J. Liu, J. Pei and Q. Chen, A hybrid model for investigating transient particle transport in enclosed environments, *Building and Environment*, vol. 62, pp. 45-54, 2013.

[15] S. Liu, L. Xu, J. Chao, C. Shen, J. Liu, H. Sun, X. Xiao and G. Nan, Thermal environment around passengers in an aircraft cabin, *HVAC&R Res.*, vol. 19, pp. 627-634, 2013.

[16] Z. Zhang and Q. Chen, Comparison of the Eulerian and Lagrangian methods for predicting particle transport in enclosed spaces, *Atmospheric Environment*, vol. 41, pp. 5236-5248, 2007.

[17] J. M. A. Hofman, Control-fluid interaction in air-conditioned aircraft cabins: A demonstration of stability analysis for partitioned dynamical systems, *Comput. Meth. Appl. Mech. Eng.*, vol. 192, pp. 4947-4963, 2003.

[18] T. Zhang and Q. Chen, Novel air distribution systems for commercial aircraft cabins, *Building and Environment*, vol. 42, pp. 1675-1684, 2007.

[19] W. Liu, C. H. Lin, J. Liu and Q. Chen, Simplifying geometry of an airliner cabin for CFD simulations, *Indoor Air Quality and Climate 2011: Proc. 12th Int. Indoor Air Quality and Climate Conf.*, Austin, Texas, 2011.

[20] J. F. Thompson, F. C. Thames, C. W. Mastin, Automatic numerical generation of body-fitted curvilinear coordinates for a field containing any number of arbitrary 2-D bodies, *J. Comput. Phys.*, vol. 15, pp. 299-319, 1974.

[21] M. M. Hefny and R. Ooka, CFD analysis of pollutant dispersion around buildings: Effect of cell geometry. *Building and Environment*, vol. 44, pp. 1699-1706, 2009.

[22] R. Löhner, K. Morgan, J. Peraire and M. Vahdati, Finite element flux-corrected transport (FEM-FCT) for the Euler and Navier-Stokes equations, *Int. J. Numer.*, vol. 7, pp. 1093-1109, 1987.

[23] A. Jameson and T. J. Baker, Improvements to the aircraft Euler method, AIAA-87-0425, 1987.

[24] V. Bianco, O. Manca, S. Nardini and M. Roma, Numerical investigation of transient thermal and fluidynamic fields in an executive aircraft cabin, *Appl. Therm. Eng.*, vol. 29, pp. 3418-3425, 2009.

[25] S. S. Isukapalli, S. Mazumdar, P. George, B. Wei, B. Jones and C. P. Weisel, Computational fluid dynamics modeling of transport and deposition of pesticides in an aircraft cabin, *Atmospheric Environment*, vol. 68, pp. 198-207, 2013.

[26] G. Yu, B. Yu, S. Sun, and W. Q. Tao, Comparative study on triangular and quadrilateral meshes by a finite-volume method with a central difference scheme, *Numer. Heat Transfer B*, vol. 62, pp. 243-263, 2012.

[27] F. Juretic´ and A. D. Gosman, Error analysis of the finite-volume method with respect to mesh type, *Numer. Heat Transfer B*, vol. 57, pp. 414-439, 2010.

[28] Y. Kallinderis, A. Khawaja and H. McMorris, Hybrid prismatic/tetrahedral grid generation for viscous flows around complex geometries. *AIAA J.*, vol. 34, pp. 291-298, 1996.

[29] Tysell, L, Hybrid grid generation for complex 3D geometries, *Numerical Grid Generation in Computational Field Simulations 2000: Proc. 7th Int. Numerical Grid Generation in Computational Field Simulations Conf.*, Whistler, pp. 337-346, British Columbia, Canada, 2000.

[30] J. Tu, G. H. Yeoh and C. Liu, *Computational Fluid Dynamics: A Practical Approach*, pp. 147-148, Butterworth-Heinemann, Oxford, 2007.

[31] Z. Zhang, W. Zhang, Z. Zhai and Q. Chen, Evaluation of various turbulence models in predicting airflow and turbulence in enclosed environments by CFD: Part 2-Comparison with experimental data from literature, *HVAC&R Res.*, vol. 13, pp. 853-870, 2007.

[32] ANSYS, ANSYS Fluent 13.0 Documentation, ANSYS, Inc., Lebanon, NH, 2010.

[33] S. R. Mathur and J. Y. Murthuy, A pressure-based method for unstructured meshes, *Numer. Heat Transfer B*, vol. 31, pp. 195-215, 1997.

[34] L. Sun, S. R. Mathur, and J. Y. Murthy, An unstructured finite-volume method for incompressible flows with complex immersed boundaries, *Numer. Heat Transfer B*, vol. 58, pp. 217-241, 2010.

[35] A. Dalal, V. Eswaran, and G. Biswas, A finite-volume method for Navier-Stokes equations on unstructured meshes, *Numer. Heat Transfer B*, vol. 53, pp. 238-259, 2008.

[36] P. V. Nielsen, Flow in air-conditioned rooms, Ph.D. thesis, Technical University of Denmark, Lyngby, Denmark, 1976.

[37] R. Kumar and A. Dewan, URANS computations with buoyancy corrected turbulence models for turbulent thermal plume, *Int. J. Heat Mass Transfer*, vol. 72, pp. 680-689, 2014.